ARTICLE

Check for updates

Trends in atmospheric methane concentrations since 1990 were driven and modified by anthropogenic emissions

Ragnhild Bieltvedt Skeie [1✉], Øivind Hodnebrog [1] & Gunnar Myhre [1]

The atmospheric methane trend is not fully understood. Here we investigate the role of the main sink, the main natural source, and anthropogenic emissions on the methane growth rate over the last three decades using numerical models and emission inventories. We find that the long-term trend is driven by increased anthropogenic methane emissions, while wetland emissions show large variability and can modify the trend. The anthropogenic influence on hydroxyl radical, through nitrogen oxides and carbon monoxide emissions, has modified the trend over the last decades and contributed to the atmospheric methane stabilization from 2000 to 2007. The hydroxyl radical increase prior to this stabilization period might have contributed to the decline in the isotopic ratio after 2007 due to the time dependent isotopic response of hydroxyl radical. Emission reductions due to COVID-19 restrictions via the influence on hydroxyl radical, possibly contributed to approximately two thirds of the increase in methane growth from 2019 to 2020.

[1] CICERO Center for International Climate Research, Oslo, Norway. ✉email: r.b.skeie@cicero.oslo.no

Methane (CH_4) is the second strongest contributor to anthropogenic greenhouse gas radiative forcing after carbon dioxide[1]. The global mean concentration reached 1908 parts-per-billion (ppb) in 2021[2], >160% higher than the pre-industrial level (year 1750) of methane and this increase is largely driven by anthropogenic activities[3].

The current atmospheric concentrations are higher than in scenarios consistent with limiting global warming to 1.5 and 2 degrees[4], and several studies point to the importance of reducing atmospheric methane to meet the temperature goals of the Paris Agreement[4–7]. To better evaluate mitigation efforts in view of reaching the temperature goals in the Paris Agreement[8], an improved understanding of past methane trends is crucial[5]. However, over the four last decades, the growth rate of atmospheric methane has varied[9] (Fig. 1) and the reasons for the variations in the observed methane trend have been discussed in the literature often with contradicting explanations (see Turner, et al.[10] and references therein). The high growth rate in the 1980s slowed down in the 1990s. Between 2000 and 2007, atmospheric methane concentrations were relatively stable, but from 2007 it started rising again[11,12], with a further acceleration in 2014[4]. Large annual increases equivalent to those observed in 2020 and 2021 (15.2 and 17.8 ppb, respectively) have not been seen since the 1980s[9].

What determines the growth rate of atmospheric methane is the imbalance in the methane budget. The global methane budget – the total sources and sinks of methane—consists of several large terms that are all associated with large uncertainties[13]. Anthropogenic sources contribute to about 60% and natural sources (mainly wetlands) to about 40 % of the total sources of methane[13]. The main sink of methane is through chemical reactions in the atmosphere. Understanding the observed changes in methane growth rates requires a good understanding of trends in the methane budget terms. The uncertainties in the components of the methane budget greatly exceed the sources-sink imbalance driving the contemporary methane trends[10]. These uncertainties are a crucial hindrance in our ability to understand past and present methane growth rates.

Anthropogenic activity is the main contributor to the increase in atmospheric methane since pre-industrial times[3], through agriculture (rice cultivation, enteric fermentation and manure management), fossil fuel activities (coal mining, oil and gas industry), landfill and waste management. For the increase in atmospheric methane since 2007 several studies point at
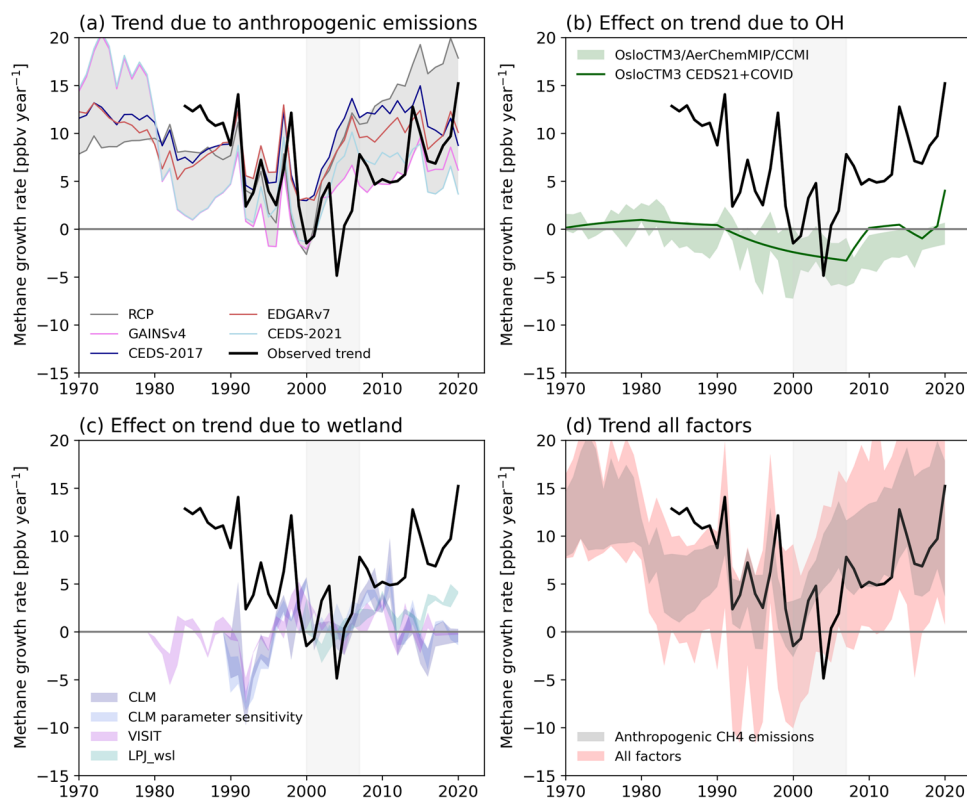
Fig. 1 Observed and calculated growth rate in atmospheric methane. In (**a**) the calculated growth rate in atmospheric methane due to different emission inventories (anthropogenic and biomass burning, see Method and Supplementary Fig. 1) from the box model are shown as coloured lines. The grey shading indicates the ranges in the calculated methane growth rate from the different emission inventories. In (**b**) the difference in the methane growth rate allowing for changes in methane lifetime (due to OH changes) over time compared to fixed methane lifetime. The green line shows contribution to the growth rate allowing for changes in methane lifetime following the OsloCTM3 CEDS21 + COVID, while the green shading indicates the range in contribution from allowing methane lifetime to change following the other OsloCTM3 CEDS17 simulations (with fixed and varying meteorology), CCMI and AerChemMIP results (see Box model section in Method). In (**c**) the difference in the methane growth rate allowing for changes over time in the natural emissions compared to fixed natural methane emissions. The different shadings indicate range in contributions from CLM driven by different meteorological data, CLM parameter sensitivity simulations, the set of VISIT model results and the set of LPJ-wsl simulations. In (**d**) the calculated methane growth rate combining different anthropogenic emission inventories, estimates of changes in methane lifetime over time and changes in natural methane emissions over time (red shading) compared to only the ranges in the calculated methane growth rate based on anthropogenic emission inventories (grey shading, similar to the shading in (**a**)). In all panels, the observed annual methane mole fraction increase from NOAA Global Monitoring Laboratory[9] are shown in black. The stabilization period from 2000 to 2007 is indicated by the grey vertical field. In Supplementary Figs. 2–4, similar figures with different base set up of the box model (methane lifetime, natural emissions) are shown.

anthropogenic emissions as the main contributor[14–17]. Different emission inventories and scenarios show large differences in emission trends, both prior to the 1990s, as well as after 2005 (Fig. 2), especially for the fossil fuel sector[18].

Wetland emissions may have decreased since pre-industrial time driven by conversion of wetland areas to drylands by humans[19] or increased in response to increased precipitation and atmospheric CO_2 that consequently increase net primary productivity and heterotrophic respiration[20]. A strengthening of the wetland methane feedback, an increase in wetland emissions driven by temperature and precipitation increases, is of concern as the climate is changing[13]. Results from one wetland model show increased wetland emissions over the last two decades driven by climate change[21]. Contrary multi-land-model studies find no trend in wetland methane emissions over the most recent decade[13]. However, land models have difficulties in representing wetlands, in particular seasonal flooding influences the temporal and spatial variability in wetland emissions[22]. Based on measurements of methane and isotopic ratio, studies point at increased biogenic emissions in the tropics as a contributor to the recent increase in methane[4,23,24] and global inversion studies find contribution from tropical wetlands[25], and regional studies do find increases in tropical wetland emissions in South America[26,27] and tropical Africa[28,29] over the last decade.

The dominant loss of atmospheric methane is through oxidation by the hydroxyl radical (OH). The abundance of OH is dependent on the combined effect of atmospheric composition and meteorological factors such as humidity, UV radiation, and temperature. OH has an atmospheric lifetime of ~1 s[30] and hence direct measurements cannot be used to derive the methane sink trend. To gain knowledge of the trend in OH and hence the methane sink, atmospheric chemical models[31–33] and inverse methods using methyl chloroform or other components[34–38] are

necessary. In chemical modelling carbon monoxide (CO) and nitrogen oxides (NO_x) emissions play an important role for the OH trend[32,33,39], as increases in NO_x tend to increase OH and increases in CO tend to decrease OH. The spread in estimates of the OH trend is large, and chemical models and inversion method show different trends for the period with renewed growth of methane[33]. Incomplete knowledge of the OH sink also impact top-down estimates of trend in methane sources using inverse modelling[39,40]. These methods mostly apply prescribed OH and hence attribute all mismatches between observations and models to emission sources.

In this study the time evolution as well as the relative roles of the methane sink, natural sources and anthropogenic sources on atmospheric methane is consistently assessed, with the focus on the last three decades. The trend in OH and hence the methane lifetime is studied using a chemical transport model (OsloCTM3), investigating both the role of meteorological factors as well as anthropogenic influence on OH through changes in NO_x and CO emissions. The possible influence on the high growth rate of atmospheric methane in 2020 due to emission reductions of NO_x and CO as a consequence of COVID-19 lockdowns are assessed. The time evolution of natural emissions is calculated using the community land model CLM5.0, and the trend in anthropogenic emissions is investigated using a wide range of emission inventories and scenarios. To assess the role of these three largest terms in the methane budget on the atmospheric methane growth rate, a box model is used. Joint changes as well as separate contributions of the methane budget terms and their uncertainties to the year-to-year increase in atmospheric methane are assessed. Another box model is used to illustrate the influence of OH on the isotopic ratio, with its time dependent isotopic response, as well as the response due to wetland and anthropogenic emissions.

Results

Anthropogenic methane emissions and influence on methane trend. Figure 1a shows how different anthropogenic emission inventories influence the growth rate of atmospheric methane. For these calculations a box model (see Method) is used, with constant methane lifetime and natural emissions while anthropogenic and biomass burning emission vary (Fig. 2). The different anthropogenic methane emission inventories (Table 1) used as input for these calculations have a large spread and show different time development (Fig. 2). Due to different start years of the inventories (Table 1), different emission inventories/scenarios are combined to cover the period 1950 to 2020 (see Method and Supplementary Fig. 1).

The box model calculations using the CEDS-2017 emission inventory and a Shared Socioeconomic Pathway (SSP) scenario
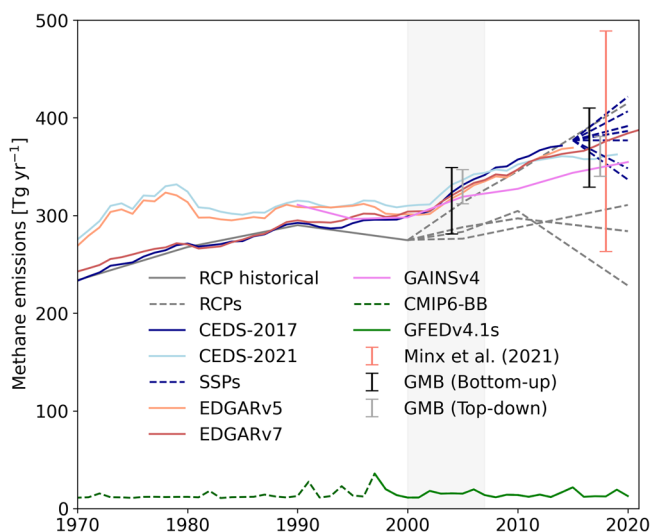
Fig. 2 Time development of anthropogenic methane emissions and biomass burning emissions from 1970 to 2020. Annual emissions for anthropogenic emission inventories and scenarios (see Table 1 for details) from 1970 and onwards and open biomass burning emissions (CMIP6-BB followed by GFED from 1997 and onwards) are shown. The ranges in anthropogenic emissions from the Global Methane Budget (agricultural and waste, fossil fuel and biofuel) for the year 2017 and the 2000–2009 period are marked by error bars (black: bottom-up estimates, grey: top-down estimates). The uncertainty estimate (±30% for 90% confidence interval)[56] is added to EDGARv7 in 2018. The SSPs are the nine CMIP6 harmonized marker scenarios in the SSP database. The stabilization period from 2000 to 2007 is indicated by the grey vertical field.

Table 1 Anthropogenic emission inventories and scenarios used in this study.

Short name	References	Start year	End year
CEDS-2021	McDuffie, et al.[94] updated	1970	2019
CEDS-2017	Hoesly, et al.[65]	1850	2014
SSPs	Gidden, et al.[95]	2015	2100
GAINSv4	Höglund-Isaksson, et al.[18]	1990	2050
RCPs	Lamarque, et al.[44] and van Vuuren, et al.[96]	1850	2100
EDGARv7	Crippa, et al.[97] and EC-JRC/PBL[98]	1970	2021
EDGARv5	Crippa, et al.[99]	1970	2015

Short name used in the text, references, start year and end year of the emission data. Links to the emission data are included in Supplementary Table 1.

(CEDS-2017 in Fig. 1a, see Method) give an increase in methane that is too small prior to 1990 and too strong post 2005 compared to the observed growth rate[9]. The CEDS-2017 inventory was prepared for the Coupled Model Intercomparison Project Phase 6 (CMIP6), while the older emission inventory (RCP) prepared for CMIP5 give similar atmospheric growth rates and an even stronger positive methane trend than CEDS-2017 over the last decade. Note that RCP follows the Representative Concentration Pathway 8.5 (RCP8.5) post 2000, while CEDS-2017 follows a scenario with small increase post 2015, and not a SSP scenario with similar emission growth as RCP8.5 (Fig. 2).

Using the more recent emission inventories (GAINSv4, CEDS-2021) in the calculations give atmospheric growth rates closer to observed at the end of 1990s to mid-2010s, with a smaller growth rate post 2000 compared to the older emission inventories (RCP, CEDS-2017). Prior to the 1990s CEDS-2021 anthropogenic emissions are not able to reproduce the high growth rate in the 1980s (Fig. 1a), as also seen directly from the relatively stable CEDS-2021 emissions in the 1980s and 1990s (Fig. 2). The CEDS-2021 inventory builds on EDGARv5 emission inventory (Fig. 2), while the most recent EDGAR inventory (EDGARv7) is similar to the older emission inventories (Fig. 2). The older emission inventories and EDGARv7 are closer to the observed growth in the 1980s than the other more recent inventories. A sensitivity test enhancing the methane lifetime due to OH from 9.6 to 11 years, gives atmospheric growth rate slightly closer to the observed in the 1980s (Supplementary Fig. 2).

A single anthropogenic emission inventory alone will never be able to reproduce the observed trend in atmospheric methane. Emissions are uncertain (see e.g., the error bars in Fig. 2) and represented here as a range of emission inventories. Observed growth rates are mostly within the range of the calculated growth rate, where the more recent inventories better reproduce observations after the stabilization period, while the older emission inventories in addition to EDGARv7 are closer to observations in the 1980s.

**OH and methane lifetime.** To study the trend in the OH sink, a chemistry transport model (OsloCTM3, see Method) is used. In Fig. 3 the OsloCTM3 results for OH are shown as changes in global OH relative to year 2000. As oxidation by OH is the main methane sink, the methane lifetime trend goes in the opposite direction of the OH trend (Supplementary Fig. 5). Two sets of simulations are performed, time-slice simulations with fixed 2010 meteorology for selected years from 1850 to 2020 and simulations with variable meteorology for the years 1997 to 2017, with the CEDS-2017 emission inventory as input (CEDS17).

The OsloCTM3 simulations show a decrease in OH (and an increase in methane lifetime) from 1850 to 1990 of ~3%. An increase in methane lifetime over this period can be expected as methane concentration more than doubled over this period, from 808 ppb in 1850 to 1717 ppb in 1990[41]. The OH in 1850 is similar as in year 2000, but in the second half of the 20th century the OH and methane lifetime were ~2–3% lower and longer, respectively, as in 1850. From 1990, OH rapidly increased up to 2007 with an increase in OH of 5.8% in the simulation with fixed meteorology.

A similar increase as in the fixed meteorology simulations is seen in the simulation with varying meteorology, but with slightly smaller magnitude (4.9 %). As expected, the results with varying meteorology show more year-to-year variability, both as meteorological factors (humidity, radiation, lightning etc.) and biomass burning emissions influence the OH distribution with large interannual variability. Considering meteorological factors, most of the increase occurs over a shorter period from 1999 to 2007 with an increase of 3.8%. Post 2007, the OH concentration declines, in the simulation with constant meteorology, while for the simulation with variable meteorology, the concentrations fluctuate around larger values than prior to the year 2000.

The increase in OH is slightly less between 2000 and 2007 using the most recent CEDS emission inventory (CEDS21) (Fig. 3b) compared to the CEDS17 simulation. For the year 2020, the CEDS21 emission for year 2019 is scaled by estimated emission reduction due to policies to combat the COVID19 pandemic (see Method). The results for 2020 show a sharp decrease in OH of 2.2% from 2019 (Fig. 3b) and hence an increase in methane lifetime.

Also shown in Fig. 3 are results from two multi-model initiatives, the Chemistry–Climate Model Initiative (CCMI)[42] and The Aerosol Chemistry Model Intercomparison Project
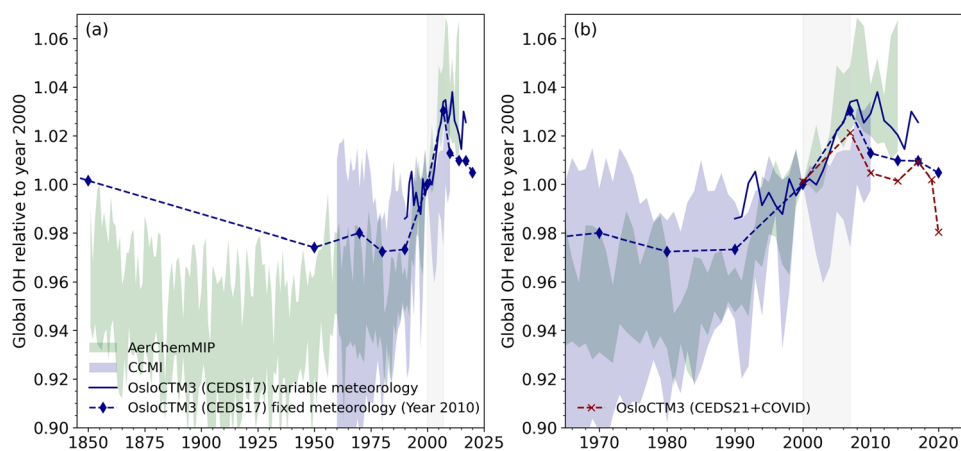
Fig. 3 Modelled global OH relative to global OH in year 2000. In (**a**) results from 1850 are shown while in (**b**) the results are shown from 1970. Results from the OsloCTM3 time-slice simulations (with fixed year 2010 meteorology) are shown as dark blue diamonds combined with dashed lines and the time development for OH from the simulations with variable meteorology are shown as a dark blue solid line. These simulations use the CEDS-2017 emissions (CEDS17). In (**b**) the additional simulation with the CEDS-2021 emissions and COVID emission for 2020 (with fixed year 2010 meteorology) is shown as dark red crosses combined with dashed line (CEDS21 + COVID). The range of the model results from AerChemMIP[33] up to 2014 are shown as green shading and model results from CCMI[31] up to 2010 are shown as blue shadings. Note that the multi-model results are tropospheric means, while the OsloCTM3 results are for the whole atmosphere. The stabilization period from 2000 to 2007 is indicated by grey shadings. Similar figures for methane lifetime are shown in Supplementary Fig. 5.

(AerChemMIP)[43] endorsed by CMIP6. The span of the relative change in OH from 11 models from phase 1 of CCMI[31] and 3 models participating in AerChemMIP[33] are shown as shadings in Fig. 3.

The emission inventories used to drive the OsloCTM3 model are the same as used in CMIP6/AerChemMIP. AerChemMIP models show similar trend in OH as OsloCTM3, with a sharp increase of around 9% in global OH from 1980 to 2014[33]. The similarities in the time evolution of these model results are linked to the emissions of chemically reactive components used to drive the models. In CCMI a different emission inventory was recommended, based on the historical emissions used in CMIP5[44] and RCP8.5[45], although some models used other emission inventories[31]. The model spread for relative OH is larger, as more model results are included, but the increase in OH since 1990 is less steep compared to AerChemMIP results, indicating a role for the emissions used for the OH time evolution (see Discussion).

OH sink and influence on atmospheric CH4 trend. To illustrate the effect of the OH trend on the methane growth rate, the lifetime due to OH in the box model (9.6 years, see Method) is adjusted based on the simulated relative change in OH from OsloCTM3, CCMI and AerChemMIP. In Fig. 1b the difference in calculated methane trend between runs with adjusted methane lifetime over time and with fixed methane lifetime are shown. Adjusting the lifetime based on results from the OsloCTM3 and the multi-model initiatives (green shadings in Fig. 1b) reduced the atmospheric trend from 1980s up to -7.3 ppb yr^{-1} in year 2000. The contribution to the trend is negative throughout the stabilization period and becomes less negative in the period with renewed growth in atmospheric methane. Changes in the OH sink have likely contributed to the stabilization of atmospheric methane in the period 2000 to 2007.

Results based on OsloCTM3 simulations with fixed meteorology are shown as a green line in Fig. 1b. After year 2000 the lifetime is adjusted based on the CEDS21 + COVID simulation and before year 2000 the lifetime is adjusted based on the CEDS17 simulations, as the trend in the emissions used in these simulations are similar before year 2000 (Supplementary Fig. 8). From 2010, the contribution from OH to the growth rate was negligible until the end of the period. From 2019 to 2020 the methane trend increased by 3.7 ppb yr^{-1} due to COVID emission reductions of NO$_x$ and CO, possibly contributing to the 5.5 ppb yr^{-1} larger observed growth rate in 2020 compared to 2019[9]. The approximately two thirds of the increase in growth rate from 2019 to 2020 is larger than previous estimates of up to one half[46] and 53 (±10) %[47].

Wetland emissions. The CLM5.0 model is used to calculate natural fluxes of methane and estimate recent trends in these fluxes (see Methods). Three sets of simulations are performed, with different meteorological data used to drive the model in addition to sensitivity tests varying two of the most sensitive parameters for methane fluxes in the CLM[48].

The global wetland emissions from the CLM are in the lower range of the Global Methane Budget (GMB) emissions[13] due to lower emissions in the tropics, while at high latitudes the CLM are in the upper range of the GMB emissions (Fig. 4). The different meteorological data used to drive the model give slightly different wetland fluxes (Fig. 4). Supplementary Fig. 6 show the net emissions that in addition to wetland emissions, defined in the CLM as emission fluxes in the inundated fraction of the grid cell, include fluxes from the non-inundated areas and soil sink. The different meteorological data used to drive the model give slightly different wetland fluxes (Fig. 4) and span a larger range for net emissions (Supplementary Fig. 6).

Varying the two parameters that are found to influence the methane fluxes the most[48] results in global wetland fluxes that span the entire range of both bottom-up and top-down estimates from the GMB (Fig. 4). The two parameters considered are q10ch4 (q10 for methane production) and f_ch4 (methane production to total C mineralization rate). The minimum, maximum and the value in the main simulations for q10ch4 are 1, 4 and 1.33 respectively. For f_ch4 the values are 0.1, 0.4 and 0.26. The minimum value of f_ch4 gave unrealistically low values for methane emissions (Supplementary Fig. 7) and is not included in Fig. 4.

Wetland emissions are highly dependent on the wetland distribution. In the CLM, the wetland extent is parameterized and optimized to fit the wetland area in Wetland Area and Dynamics for Methane Modelling (WAD2M) dataset[49] (see Method). The wetland emissions are also calculated based on the CLM wetland fluxes (calculated in each grid-cell and independent of wetland area) and the monthly wetland area in WAD2M and its predecessor the hybrid wetland product SWAMPS-GLWD[50]. As the wetland area in SWAMPS-GLWD was larger than in the updated and improved WAD2M dataset[49], the wetland emission using SWAMPS-GLWD was larger than WAD2M (Fig. 4 third column). Also note that the wetland fluxes multiplied by the monthly global wetland distribution (WAD2M) gave similar results to the CLM where wetland area is parameterised based on the same wetland distribution.

The total soil sink does not have large year-to-year variability, does not vary for different meteorological datasets, and is not influenced by changing the two parameters in the CLM (Fig. 4).

In Fig. 5. the trend in natural fluxes of methane is shown as global anomalies of net methane emissions (wetland emissions, fluxes from non-inundated areas and soil sink) (Fig. 5a) and for only wetland emissions (Fig. 5b). The general pattern in the time evolution is similar for the CLM model driven by different meteorological datasets, where the global net-emission increased from 1992 to 2000, then increased again from the end of the stabilization period up to 2011 and decreased thereafter (Fig. 5a). The year-to-year variability in the net methane emissions can be related to the phase of the El Nino-Southern Oscillation. In the CLM there are positive anomalies for La Nina years (around year 2000, 2007-12) and negative anomalies for El Nino years (1992,1998,2016) (Fig. 5a).

The anomalies scale with total emissions. As GSWP3 has the largest emissions, a larger year-to-year variability than CRUN-CEP and CRUJRA is seen. A larger year-to-year variability is also seen in the parameter sensitivity results (pink shading in Fig. 5), where the total global wetland fluxes span the range from 100 to 200 Tg yr^{-1} (Fig. 4). The parameter sensitivity tests do not change the overall trend, but the magnitude of the emissions and hence the amplitude of the anomalies (Supplementary Fig. 7).

The interannual variability in the wetland emissions are smaller than for the net emissions (Fig. 5), as the emissions in the non-inundated areas included in the net emissions are more affected by meteorological factors. The general pattern for wetland emissions is similar to the net-emissions, with negative anomalies prior to the stabilization period, and positive anomalies in the period with the renewed growth in atmospheric methane (Fig. 5b). Using the wetland area distribution directly in combination with CLM wetland fluxes give similar results as the CLM parameterisation, but there are some small differences. Between 2011 and 2014, emissions are stable if wetland area data are used while for the parameterisation the emissions increased.

Added to Fig. 5b are the Vegetation Integrated Simulator of Trace gases (VISIT) model results[16] using two different schemes
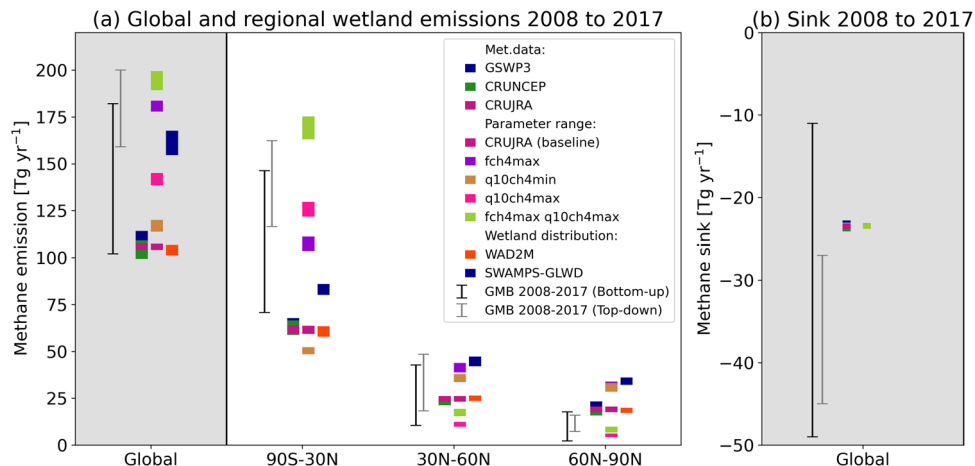
Fig. 4 Modelled wetland methane emissions and soil sink. In (**a**) global and regional wetland emissions and in (**b**) the global soil sink calculated using the CLM model are shown. Coloured boxes show the annual mean values from the CLM simulations for the period 2008–2017 (or the end year of the simulation see Method) compared to the range of reported studies in The Global Methane Budget (GMB) for the 2008–2017 decade from top-down inversions models and bottom-up models[13] represented by the error bars. The CLM results are presented for three groups, simulations driven by different meteorological data (left column), simulations driven by CRUJRA meteorological data where values for two central parameters for methane fluxes (q10ch4: q10 for methane production and f_ch4: methane production to total C mineralization rate) are varied (middle column) and methane fluxes calculated using the monthly wetland distributions and the methane fluxes for wetland areas from the CLM (right column). Note that some of the coloured boxes overlap.

to estimate the wetland emissions and The Lund-Potsdam-Jena-Wald, Schnee and Landschaft (LPJ-wsl) model results driven by two different meteorological datasets[21]. The time development in VISIT show similarities to the CLM results, both having 1992 as the lowest value and an increase (less negative anomalies) up to the end of the 1990s and in general positive anomalies after the stabilization period. The VISIT model shows larger interannual variability but note that the total fluxes are larger compared to the CLM (Fig. 5b). The LPJ-wsl results[21] show an increase in emissions from the stabilization period and up 2021.

Influence of natural emissions on atmospheric methane trend. Adding interannual variability in natural emissions of methane alters the atmospheric methane growth rate calculated by the box model (Fig. 1c). As the total global emissions are uncertain, the anomalies are scaled to a mean value of 149 Tg yr^{-1}, the best estimate from GMB bottom-up studies[13]. The net emission anomalies from CLM simulations (Fig. 5a) and wetland flux anomalies (Fig. 5b) from VISIT runs and LPJ-wsl runs are used. If the total natural emissions are increased, and the anomalies scaled by a larger number of 179 Tg yr^{-1}, slightly larger contribution to the atmospheric methane trend are found (Supplementary Fig. 4) compared to results in Fig. 1.

The CLM and VISIT simulations show a negative contribution to the atmospheric methane trend in the early 1990s (Fig. 1c). The observed atmospheric methane trend is weakening in the 1990s compared to the 1980s, and the negative anomalies in the natural fluxes might have contributed to this. The three models show an increased contribution to the trend in the first years following the stabilization period, indicating a possible wetland contribution to the rapid growth in methane from 2007. The LPJ-wsl results show an increasing contribution to the growth rate for the recent decade, while the contribution to the trend is small for CLM and VISIT. Note that anomalies are set to zero after end of land model results (2014,2016 and 2019 for CLM and 2016 for VISIT, Supplementary Fig. 9b).

Combined influence on atmospheric methane trend. In the previous sections the effect on the atmospheric growth rate due to different anthropogenic emission inventories, changes in the

methane sink over time and changes in natural fluxes is illustrated separately. If all these effects are combined, the observed trend is well within the modelled range over the last two decades (except the negative anomaly in 2004) (Fig. 1d). In the 1980s and 1990s the modelled growth rates are generally lower than the observed growth rates. In the estimates considered here, changes in methane lifetime due to OH have contributed to the reduced growth rate of methane in the 1990s and the stabilization period 2000 to 2007. Both OH and the modelled natural fluxes made a positive contribution to the trend in the years following 2007, and possibly contributed to the renewed growth in methane. The main contributor to the atmospheric methane trend is anthropogenic methane emissions, but changes in OH and wetland emission can modify the trend.

Influence on $\delta^{13}C_{CH4}$ trends. Measurements of methane isotopes can indicate changes in methane sources as biogenic, thermogenic and pyrogenic sources are characterized by different isotopic signatures[51]. Isotope measurements can also indicate changes in the oxidation capacity of the atmosphere as OH preferentially oxidizes the $^{12}CH_4$ methane isotope. Prior to the stabilization period the observed trend in $^{13}C/^{12}C$ isotopic ratio ($\delta^{13}C_{CH4}$) was positive, while at the end of the stabilization period, the trend in $\delta^{13}C_{CH4}$ turned negative[4].

Nisbet, et al.[4] pointed at several possible reasons for the more negative values in atmospheric $\delta^{13}C_{CH4}$ since 2007, one of them was a decline in the atmospheric oxidation capacity. Here we propose an alternative hypothesis that an earlier increase in the oxidation capacity of the atmosphere can decrease the isotopic ratio in later years. Both Haghnegahdar, et al.[52] and Stell, et al.[53] (in their Fig. S9) illustrated that the isotopic effect of a step change in OH exhibited a sign change in $\delta^{13}C_{CH4}$ trend after around one decade. We investigate the isotopic effect of the strong increase in OH prior to the stabilization period by using an isotopic box model (see Method).

Results show indeed that about 30% of the strong observed decrease in $\delta^{13}C_{CH4}$ of 0.2‰ between 2008 and 2014 can be explained by OH from OsloCTM3 and AerChemMIP driven by CEDS emissions (Fig. 6a; Supplementary Fig. 10). The further observed decline of >0.2‰ in $\delta^{13}C_{CH4}$ between 2014 and 2020[2] is
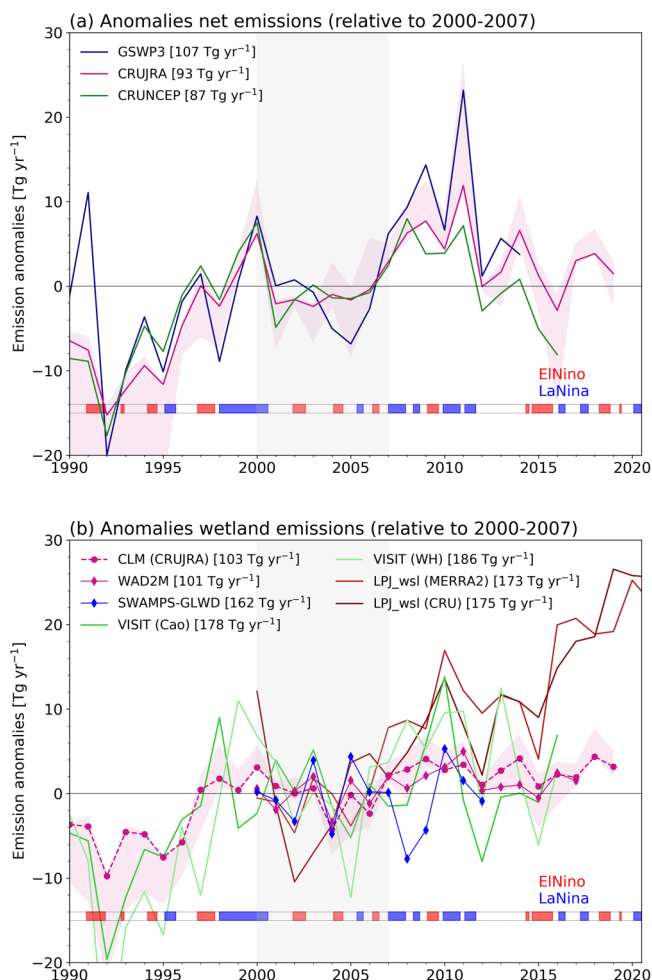
Fig. 5 Global anomalies for natural methane emissions. In **a** global anomalies for net methane emissions (wetland emissions, fluxes from non-inundated areas and soil sink) and in **b** global anomalies for wetland emissions from 1990 to 2019. Total global emissions for the baseline period (2000–2007) are indicated in the legend. The El Nino-Southern Oscillation phases are indicated with El Nino (red) and La Nina (blue) from the Oceanic Niño Index (NOAA. https://www.cpc.ncep.noaa.gov/data/indices/oni.ascii.txt (2023)) with threshold of +0.5 deg for El Nino and −0.5 for La Nina where tick marks on x-axis indicate mid-year. In **a** annual emission anomalies from the CLM using three different meteorology datasets to drive the model are shown. Pink shading indicates the range of anomalies from simulations varying two parameters in the biogeochemical model using the CRUJRA meteorology. In **b** the main CLM results are compared to CLM wetland fluxes combined with WAD2M (red diamond) and SWAMPS-GLDW (blue diamond) datasets for wetland distribution, and compared to the VISIT model results[16] and LPJ-wsl model results[21]. The stabilization period from 2000 to 2007 is indicated by grey shadings.

not explained by the OsloCTM3 (CEDS21 + COVID). However, results using the AerChemMIP and CCMI datasets indicate that the OH evolution prior to this period has led to a small decline in $\delta^{13}C_{CH_4}$ in recent years, as OH concentration is set constant after 2014 and 2010 respectively. The enhanced OH from the 1980s towards the stabilization period in AerChemMIP and OsloCTM3 contributed slightly to the increase in isotopic ratio from the late 1980s to the late 1990s. The box model simulations show relatively small influences of OH between 1998 and 2008, a period when observed $\delta^{13}C_{CH_4}$ value is also relatively constant.

The more negative values in atmospheric $\delta^{13}C_{CH_4}$ since 2007 can also indicate an increase in isotopically very negative biogenic
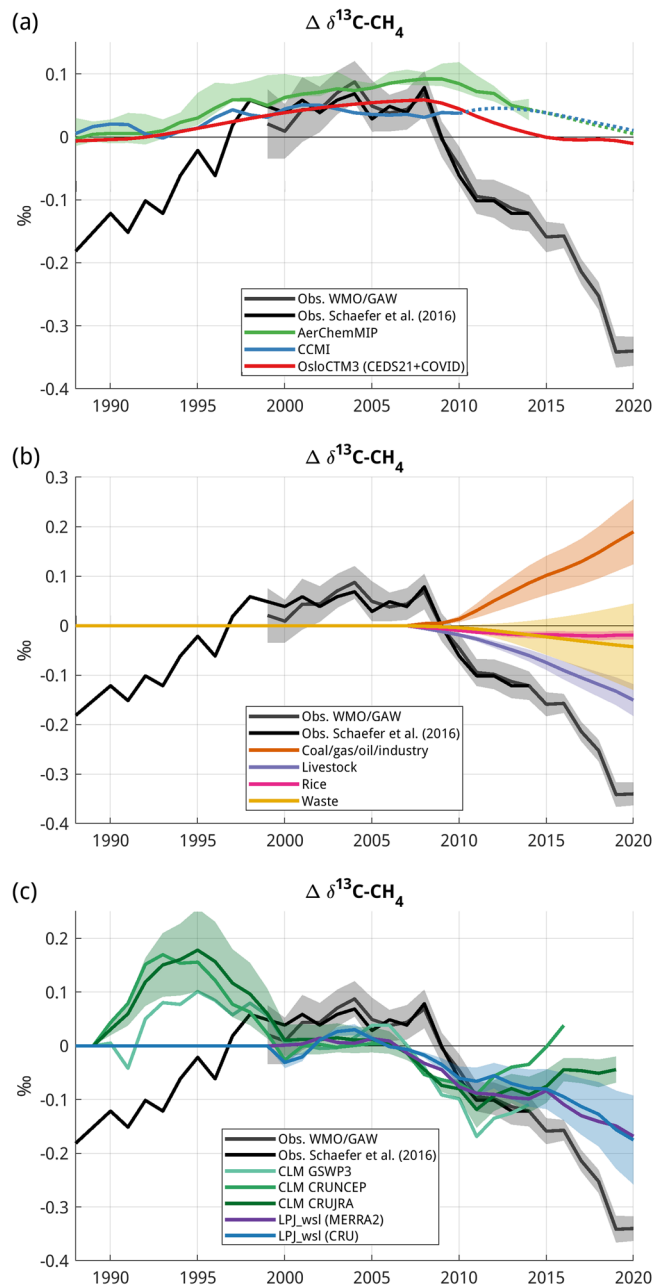
Fig. 6 Modelled influence of evolving OH concentrations and individual emission sectors on the $\delta^{13}C_{CH4}$ isotopic ratio. Anomaly in globally averaged $\delta^{13}C_{CH4}$ (‰) from observations and from the difference between box model simulations (see Methods and Supplementary Fig. 10) that are run with evolving vs. constant (**a**) OH concentrations, (**b**) anthropogenic emissions (from 2007), and (**c**) wetland emissions. In (**a**), three different OH datasets have been used (AerChemMIP, CCMI and OsloCTM3), and the green shading represents the range for the three different AerChemMIP models while dotted lines assume constant OH for the remaining time period (CCMI and AerChemMIP datasets end in 2010 and 2014, respectively). In (**b**) and (**c**), shading represent +/−1σ uncertainty in the isotopic signature for individual anthropogenic emission sectors (**b**) and wetland emissions (**c**). Observations are from Table S4 in Schaefer, et al.[100] (black line) and WMO/GAW[2] (grey line and shading).

emissions, whether from wetlands, ruminants, waste or all of these[4]. With the isotopic box model, we have quantified the contribution from evolving vs. constant emissions from individual sectors to the isotopic ratio (Fig. 6b, c; Supplementary

Fig. 11). Among the anthropogenic emissions, results show that increasing fossil emissions (isotopically less negative) have contributed a ~ 0.2‰ increase in isotopic ratio since 2007 and increasing livestock emissions (isotopically strongly negative) have contributed to a ~ 0.15‰ decrease (Fig. 6b). There is a further contribution of ~−0.05‰ from increasing waste emissions while rice emissions only contribute slightly due to near-constant emissions since 2007. It is worth noting that the contribution due to waste emissions is particularly uncertain due to large uncertainty in its global isotopic signature (yellow shading in Fig. 6b). Based on these results, a potential overestimation in the increase of fossil emissions, or under-estimation in the increase of livestock emissions, would have contributed to a more negative $\delta^{13}C_{CH_4}$ evolution. In fact, the CEDS-2021 emission inventory does show much smaller increase in both fossil and livestock emissions compared to EDGARv7 (Supplementary Fig. 11), and isotopic box model simulations using anthropogenic emissions from CEDS-2021 therefore show much smaller contributions to the $\delta^{13}C_{CH_4}$ evolution from these two sectors (Supplementary Fig. 12), indicating that uncertainties in the time evolution of anthropogenic emissions contribute to the difficulty in reproducing the observed $\delta^{13}C_{CH_4}$ evolution.

The evolving vs. constant wetland emissions (isotopically strongly negative) show small contributions to the atmospheric $\delta^{13}C_{CH_4}$ evolution during 2000–2007 and a contribution towards decreasing $\delta^{13}C_{CH_4}$ in the following few years (Fig. 6c). From around 2010 to 2020, the contribution from wetlands differs depending on the emission datasets, and interestingly, the two LPJ-wsl emission timeseries[21] show a relatively strong contribution of a ~ 0.1‰ decline in $\delta^{13}C_{CH_4}$ during this period. It should be mentioned, however, that most of the increase in wetland emissions in their inventories origin from tropical wetlands, which are less negative in $\delta^{13}C_{CH_4}$ compared to wetlands in temperate and boreal vegetation[54]. Hence, the decline of ~0.1‰ due to wetlands may be too strong in our isotopic box model, which uses one global mean value for the isotopic signature of wetland emissions.

Discussion

In this study we focus on three of the most important and uncertain factors for the methane trend over the last decades, the main sink of methane through oxidation by OH, natural emissions from wetlands and anthropogenic emissions.

As illustrated in Fig. 2, the various anthropogenic emission inventories differ in magnitude and have experienced different time evolution. The error bars from GMB in Fig. 2 are mainly based on the range of different estimates, excluding uncertainty in emission factors and activity data. For the EDGAR emission inventory these uncertainties are assessed to be −33% to +46% (at 2σ) for total anthropogenic methane emissions[55], and based on best value judgement narrowed to ±30% (90% confidence interval)[56], corresponding to 263 to 489 Tg (for 2018 in EDGARv7, Fig. 2). There are no uncertainty estimates for historical emissions and only two different emission paths prior to 1990 exist (note that emission inventories are not independent). Only the EDGARv7 inventory includes emission for year 2020, when observed methane growth rate hits a new record (Fig. 1). Driven by the agricultural and waste sector, the EDGARv7 emissions increased by 1% from 2019 to 2020, whilst others estimate a weak decrease in anthropogenic methane emissions due to COVID lockdowns[57]. McNorton, et al.[58] found increased emissions in 2020, especially from the energy sector[58], and pos-sible reasons are increased venting due to reduction in energy demand and limited maintenance during lockdown[59]. Gas lea-kages and leakages due to accidents in the oil and gas sectors are

mostly unaccounted for in the inventories and can contribute substantially to the emissions[60] and add additional uncertainties to the inventories. Noting that the different emission inventories do not span the full uncertainty in anthropogenic methane emissions, the box model results with different anthropogenic emissions illustrate the importance of anthropogenic emissions in driving the decadal increase in atmospheric methane, as also highlighted in previous studies[14–17].

Several factors influence the OH distribution and trend and hence the methane lifetime[32,61,62]. Factors that enhance OH are increased humidity, tropospheric ozone, NO_x emissions and UV radiation (influenced by stratospheric ozone). Factors that decrease OH are increased abundance of methane, CO and other compounds that have OH as their main atmospheric sink.

The AerChemMIP models and the OsloCTM3 had similar time evolution of OH (Fig. 3). As these models were driven by the same emission inventory of chemically reactive gases, this indi-cates that the emission inventories used are important for the OH variability, as also pointed out by Stevenson, et al.[33] for Aer-ChemMIP. The results from the OsloCTM3 simulation with varying meteorology show more year-to-year variability than with fixed meteorology but similar long-term trend in OH (Fig. 3b).

Dalsøren, et al.[32] investigated the drivers of the change in methane lifetime in the OsloCTM3 model and found the ratio of NO_x/CO emission to be a key variable. When the NO_x/CO ratio increases, OH production (NO_x emissions) dominates over OH loss (CO emissions) and OH concentration increases, and methane lifetime decreases. The NO_x/CO ratio increases for CEDS-2017 (Fig. 7) from 1980 to 2007 consistent with the increase in OH in the model simulations using these emissions (Fig. 3).

The time evolution of the NO_x/CO ratio differs for different emission inventories (Fig. 7). From the 1980s–1990s, the RCP and ECLIPSEv6 have weaker increase compared to the others, while EDGARv5 has the strongest increase. After the methane stabili-zation period the ratios are relatively flat for all inventories. In CCMI the emission inventory used is based on the RCP historical[44] extended by RCP8.5. This inventory has a less steep increase in the ratio from the 1980s and onwards compared to
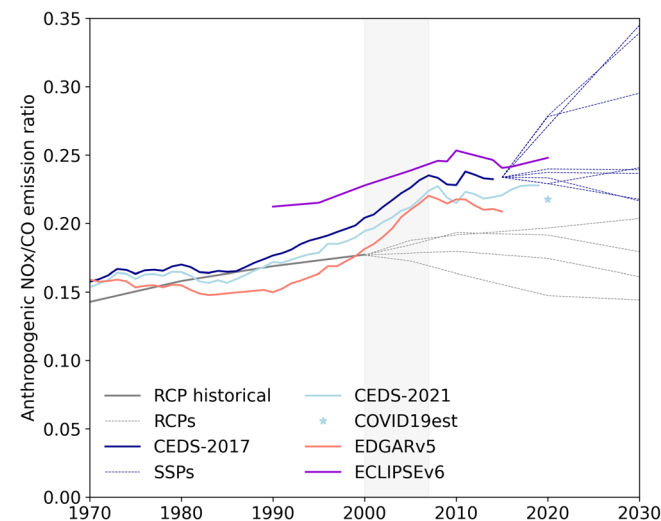
Fig. 7 Time evolution of total anthropogenic NO_x to CO emission ratios from 1970 to 2030. Details of the inventories and scenarios are presented in Table 1 and see Supplementary Fig. 8 for the NO_x and CO emissions separately. The COVID19 estimate is described in the method section. The ECLIPSEv6 used in Whaley, et al.[101] are equivalent NO_x and CO emissions to the GAINS methane emissions in Table 1. The stabilization period from 2000 to 2007 is indicated by grey shading.

CEDS-2017. The CCMI model results driven by RCP emissions have generally a weaker trend in OH from 1990s to 2010 compared to OsloCTM3 and AerChemMIP driven by CEDS-2017 emissions (Fig. 3b). Nicely, et al.[63] considered various factors affecting tropospheric OH and found the oxidizing capacity to be steady since 1980 but note that the effect of NO_x was based on model results using the RCP emission inventory. For the recent update of CEDS, both CO and NO_x emissions are revised downwards, but the NO_x/CO ratio shows similar trend as the previous CEDS inventory, as also seen as similar OH trend in OsloCTM3 simulations driven by the two inventories (Fig. 3b).

The model results using the CEDS-2017 emission inventory points at an important contribution of changes in OH via anthropogenic NO_x and CO emissions to the methane stabilization period. Several previous studies have indicated an important role of an increased methane sink for the methane stabilization period using observationally derived OH concentration[36,37,64] without presenting a physical explanation of the OH trend. However, it should be noted that the uncertainties in global anthropogenic emissions of NO_x and CO are large. These are not assessed but assumed to be >15% and less than factor of two in CEDS-2017 on a global scale[65]. The different trend of the NO_x/CO emission ratio reflects some uncertainty in methane lifetime due to uncertainties in these emissions, with both stronger (EDGARv5) and weaker (RCP) trends from 1990 to 2007 compared to CEDS-2017.

One out of several possible reasons for the more negative values in atmospheric $\delta^{13}C_{CH4}$ since 2007, is a decline in the atmospheric oxidation capacity[4]. From model simulations, driven by CEDS-2017 emissions, there is no large decline in the oxidation capacity from mid-2000s, and the NO_x/CO emission ratio from other inventories do not indicate any large change in OH either since 2007 (Fig. 7). Here we have proposed an alternative hypothesis that an earlier increase in the oxidation capacity of the atmosphere can decrease the isotopic ratio in later years, as previously illustrated for idealized step changes in OH[52,53]. Using an isotopic box model, the increase in OH from the 1980s to early 2000s using CEDS-2017 emissions can explain part of the decrease in observed $\delta^{13}C_{CH4}$ from 2007, due to the time dependence of the $\delta^{13}C_{CH4}$ response (Fig. 6). Rigby, et al.[36] also used a box model to show that evolving OH concentrations, inferred from methyl chloroform (CH_3CCl_3) observations by inversion, could explain some of the decline in $\delta^{13}C_{CH4}$ (their Fig. S6), but their inferred OH concentration had both an increase until around 2005 and a decrease thereafter. On the other hand, Lan, et al.[66] did not find an influence of OH on the $\delta^{13}C_{CH4}$ decrease, but they only explored a scenario with negative OH trend after 2006. It should be noted that box models have important limitations. Our isotopic box model is based on global and annual means and does not account for the highly variable OH concentrations in both time and space, nor the inhomogeneous distribution of the isotopic ratio and emission signatures. Further studies are needed using 3-D models to better resolve and understand the influence of OH and its temporal evolution on the $\delta^{13}C_{CH4}$ evolution.

Increased tropical wetland emission has been suggested as a reason for the renewed growth of atmospheric methane and the decline in $\delta^{13}C_{CH4}$[4,23,24]. The CLM land model results show contribution to the interannual variability in the methane growth rate, but no long-term trend. This is consistent with global biogeochemical modelling done within GMB, with no trend in emissions from 2000–2006 to 2017[14], however the uncertainties are large. Top-down estimates within GMB show relatively unchanged natural emission over the same period. Methane emissions from wetlands are strongly dependent on the wetland distribution (Figs. 4 and 5). Any trend in wetland extent will

influence the trend in methane fluxes. There is no trend in wetland extent in the WAD2M dataset[49]. As these data are used in GMB and this study, it explains the lack of long-term trend in emissions. There are however large uncertainties in the WAD2M over tropical areas, due to large seasonality and interannual variability in inundated area and vegetated forest canopy that may lead to underestimation of wetland area from satellite-based products[49] and trends in wetland area extent here can be missed. Using a hydrological model to determine the wetland area, Zhang, et al.[21] modelled an intensification of the tropical wetland methane emissions over the period 2000 to 2021, due to climate change, and highlighted the needs for sustained observations for documenting trends and variability in these emissions. Using these wetland emissions in the box models does indeed indicate that increased wetland emissions have contributed to the increase in the methane growth rate (Fig. 1c) and to the declining $\delta^{13}C_{CH4}$ in the most recent years (Fig. 6c). Emissions from livestock and waste also have strongly negative isotopic signature and increasing emissions in recent years, and the box model further indicates contributions from these two sectors on the decline in $\delta^{13}C_{CH4}$ (Fig. 6b). The comprehensive analysis of modelled versus observed $\delta^{13}C_{CH4}$ by Lan, et al.[66] identified a few scenarios that could explain the renewed methane growth after 2006, and these involved different combinations of increased wetland emission, more moderately increasing fossil fuel emissions, decreases in biomass burning emissions and/or a significant decrease in soil sink.

Other natural methane sources as emissions from freshwater systems and geological sources, are largely uncertain and temporal changes are not available in the literature[14] and hence not included here.

A single process is not sufficient to fully explain the atmospheric methane trend over the last decades. The growth rate of methane is determined by the balance of sources and sinks in the global methane budget, that are associated with large uncertainties[13]. Even small changes can have a large impact on the growth rate[10]. The main driver of the methane trend is anthropogenic activity. Mainly directly through methane emissions, but also indirectly by emissions of CO and NO_x changing the atmospheric oxidation capacity and hence the methane lifetime. There are uncertainties in both the magnitude and the trend of anthropogenic emissions, and better knowledge of emissions, both the recent emissions but also for the past, is crucial for our understanding of the methane trend. In 2020, the COVID restrictions reduced the NO_x and CO emissions. Using estimates for emission reductions in 2020, the methane lifetime increased, and possibly contributed to approximately two thirds of the increase in methane growth from 2019 to 2020. The atmospheric growth in methane in 2020 and 2021 is higher than in the early 1980s. To limit global warming, it is important to limit the growth in methane, and mitigate atmospheric constituents that influence methane indirectly by affecting the methane lifetime such as CO. The most recent anthropogenic emission estimates of methane show growth in recent years. It is critical to reverse this trend to achieve the temperature goals of the Paris Agreement.

Method

OsloCTM3. To calculate changes over time in OH and methane lifetime the OsloCTM3 is used. OsloCTM3 is an offline global three-dimensional chemistry transport model driven by 3-h meteorological forecast data by the Open Integrated Forecast System (Open IFS, cycle 38 revision 1) at the European Centre for Medium-Range Weather Forecasts (ECMWF). The OsloCTM3 consists of a tropospheric and stratospheric chemistry scheme[67] as well as aerosol modules for sulphate, nitrate, black carbon,

primary organic carbon, secondary organic aerosols, mineral dust and sea salt[68].

In this study, the model is run with anthropogenic and biomass burning emissions provided for the Coupled Model Intercomparison Project Phase 6 (CMIP6). For the years since 2000, the model is also run with a recent update of these emissions. Two sets of simulations are performed using the CMIP6 emissions, time-slice simulations for the years 1750, 1850, 1950, 1970, 1980, 1990, 2000, 2007, 2010, 2014, 2017, and 2020, with fixed year 2010 meteorological data for all simulations and a set of simulations from 1990 to 2017 with meteorological data for the corresponding year. In addition, simulations are performed for a shorter period (from year 2000) where the anthropogenic emissions are replaced by the updated version of these emissions and consistent emissions for 2020 that include COVID perturbation to the emissions. Time slice simulations with fixed meteorology (2010 meteorology) for year 2000, 2007, 2010, 2014, 2017, 2019 and 2020 are performed. Natural emissions are kept the same for all years in all simulations, except lightning emissions of NO_x. The parameterization of lightning NO_x emissions are described in Søvde, et al.[67]. The climatological mean lightning emissions is 5 Tg(N) yr^{-1} but change daily and yearly due to meteorology. The horizontal resolution is ~2.25° × 2.25° with 60 vertical layers ranging from the surface up to 0.1 hPa.

The emissions provided for CMIP6 are the historical anthropogenic emissions from the Community Emissions Data System (CEDS)[65] and biomass burning emissions from van Marle, et al.[69] (CMIP6-BB). The anthropogenic emissions are provided for the period 1750 to 2014 and extended by emissions from a scenario from 2015 to 2020, the IAMC-MESSAGE-GLOBIOM-ssp245 scenario (SSP245)[70]. For the years between 2015 and 2020, the monthly emissions are linearly interpolated. Biomass burning emissions used are CMIP6-BB with monthly resolution, while daily Global Fire Emissions Database version 4 with small fires (GFEDv4s)[71] emissions are used after 2003 in the simulation with varying meteorology. Note that CMIP6-BB are based on GFED. For the year 2020 in the fixed meteorology simulation, the open biomass burning data from SSP245 is used. The simulations using these emissions are named CEDS17.

For the simulation with updated emissions, CMIP6 anthropogenic emissions are replaced by the recent updated CEDS emissions (v_2021_02_05)[72], that extend to 2019. To create a consistent emission inventory for 2020, the CEDS emissions for year 2019 is scaled (by sector, month and grid box) by the relative reduction in the COVID-MIP emissions[73,74]. The daily emissions from GFEDv4s are used in both sets of simulations for all years. The simulation sets using these emissions are named CEDS21 or CEDS21 + COVID.

The CTM is run with prescribed surface concentrations of methane[67] scaled to the historical global mean methane concentrations[41] for the year simulated. The main atmospheric sink of methane is due to OH, mainly in the troposphere. In OsloCTM3, the loss of methane due to O(1D) and Cl is only calculated in the stratosphere. Different diagnostics of global methane lifetime and OH concentrations are available[67]. Here, we calculate OH concentration using a methane averaging kernel (OH concentration is weighted by air mass and by the loss rate to methane) from the model surface up to the model top and the methane lifetime with respect to OH for the same domain.

CLM. For calculation of natural methane fluxes, mainly methane fluxes from wetland, we apply the Community Land Model version 5.0 (CLM5)[75], the land component of the Community Earth System Model (CESM)[76]. The model includes a biogeochemical model[77,78] that simulates methane production,

oxidation, ebullition, transport through plant aerenchyma and both aqueous and gaseous diffusion. The model does not have a wetland plant functional type. Wetland area, the inundated fraction of the grid box, are specified by parameterization that include hydrological variables and parameters fitted to match satellite-based products of inundated area[78]. In the CLM5, two parameters are optimized for each grid cell based on linear equation involving simulated total water storage (TWS) to estimate inundated area[79]. Here, these parameters are re-optimized based on the global Wetland Area and Dynamics for Methane Modelling (WAD2M) dataset[49]. The two parameters are estimated for each month compared to annual values in the default CLM5.0 version. The WAD2M data for wetland areas have no value when snow on ground. If the value in a grid box is <80% of the median values in the grid box over the entire period, the value used to estimate the data are set to the mean of the values that are >80% of the median for the entire period.

A few modifications to the default setup of CLM5.0 (within cesm2.1.1-rc.05) are done. (1) The effect on methane production on soil pH are turned on, that are known to reduce the methane fluxes in the CLM model[77]. Fields of soil pH from the Harmonized World Soil Database[80] are used. (2) Set the parameter value f_ch4 (baseline fraction of anaerobically mineralized carbon atoms becoming methane) to 0.26 as used as default value in Müller, et al.[48] (3) Neglect aerenchyma transport in the non-inundated areas of the grid box[19,77]. (4) Ignore the use of a perched water table depth (water table depth above frozen soil layers) in the methane production as it gives an unrealistic spring peak in emissions in non-inundated areas at high latitudes. (5) Emissions from rice paddies are excluded from the CLM methane fluxes. Methane fluxes from lakes are not calculated.

Simulations are performed with three sets of meteorological data. Global Soil Wetness Project 3 (GSWP3) version 1 and of the CRUNCEP (version 7) are standard atmospheric data sets used to force the CLM[81]. The CRUJRA (CRU JRA v2.1)[82], data are adapted to the format used in CLM and span the more recent years. The model resolution is 0.9° × 1.25°. The CLM model is run with these three meteorological data from 1990 to the last year available (GSWP3: 2014, CRUNCEP: 2016, CRUJRA: 2019). The model runs are initialized with a field generated by simulating year 1990 for 20 years from the corresponding default CLM year 2000 initialization field (for CRUJRA the CRUNCEP field are used).

Box model. To illustrate the impact of the time development of OH and wetland emissions, as well as different anthropogenic methane emissions inventories (Fig. 2 and Table 1) on the atmospheric methane trend, a box model representing the mass balance equation is used.

The atmospheric concentrations are calculated based on time series of total methane emissions and assumptions on methane lifetimes. For conversion of emissions to mixing ratio a factor of 2.84 Tg ppb^{-1} is used. This value is calculated from the molecular weight of methane (16.04 g mol^{-1}), molecular weight of air (28.97 g mol^{-1}) and the total dry air mass of the atmosphere (5.1352e18 kg[83]). The methane loss is calculated by a set of three different lifetimes of 9.6 years, 120 years, and 160 years, representing the loss due to OH, loss in the stratosphere and soil sink respectively[84]. This give a total lifetime of ~8.4 years, within the range 9.1 ± 0.9 years in Szopa, et al.[30].

The box model is run from 1950 to 2020 for a range of anthropogenic methane emissions inventories (see Table 1). To cover the full time period, the chosen set of anthropogenic emissions are combined: RCP: RCPhistorical+RCP8.5, GAINSv4: CEDS-2021 (scaled to match start year of GAINSv4)+GAINSv4,

CEDS-2017: CEDS-2017 + SSP (REMIND-MAGPIE - SSP5-34-OS), EDGARv7, CEDS-2021: CEDS-2021 and emission in 2020 equal emission in 2019. For those anthropogenic emissions with start year 1970, CEDS-2017 scaled to match the 1970 emissions are added prior to 1970. The anthropogenic emissions used in the box model are shown in Supplementary Fig. 1.

The emissions of methane from fires are taken from GFED from 1997 to 2020 (preliminary data post 2016)[71,85] and prior to 1997 from CMIP6-BB[69] (see Fig. 2). Note that CMIP6-BB was built on GFED post 1997. The combined anthropogenic and biomass burning emissions used in the box model are shown in Supplementary Fig. 9a.

To account for changes in methane lifetime, the lifetime representing the loss due to OH (9.6 years) is scaled by a time varying factor. The scaling factor is calculated using the annual varying methane lifetime diagnosed from the OsloCTM3 simulations and tropospheric OH concentrations from the AerChemMIP (used the multi-model mean) and CCMI model (used the multi-model mean, multi-model max and multi-model min) results relative to year 2000. The scaling factor is hence 1 in 2000. The OsloCTM3 results using varying meteorology are extended in time and from 2017 to 2020 using the trend in the simulations with fixed meteorology. The OsloCTM3 CEDS21 is extended back in time from 2000 using the CEDS17 results, as trend in NO_x and CO emissions are similar prior to year 2000 in CEDS-2021 and CEDS-2017 (Supplementary Fig. 8). For CCMI and AerChemMIP the scaling factors are kept constant after model end, post 2010 and post 2014, respectively, as well as before 1960 for CCMI. The scaling factors used in the box model are shown in Supplementary Fig. 9c.

Natural emission is a large source of methane, and an important source of uncertainty in the methane budget[13]. The default natural methane emission in the box model is set to a constant value of 215 Tg yr^{-1}. This is close to the sum of the top-down estimates of wetlands (181 Tg yr^{-1}) and other natural sources including inland waters, geological, ocean, termites, wild animals, permafrost, vegetations (37 Tg yr^{-1}) from the global methane budget 2008–2017[13].

Anomalies in natural emissions for the different CLM simulations, VISIT simulations[16] and LPJ-wsl simulations[21,86] (with baseline as the period 2000–2007) are added to the natural emissions of 215 Tg yr^{-1}. As the total methane emissions from wetlands is associated with large uncertainties, the anomalies are scaled according to the bottom-up estimates from the Global Methane Budget of 149 Tg yr^{-1} from wetlands[13]. The anomalies are set to zero before and after the period with land model results. The total natural emissions including the anomalies used in the box model are shown in Supplementary Fig. 9b.

The box model is used for illustration of the effect on year-to-year increase in atmospheric methane and the relative role of anthropogenic emissions, changes in oxidation capacity of the atmosphere and wetland emissions and does not take into account complex interaction of chemistry, dynamics and spatial and temporal variability in emissions.

Box model for isotopes. Another box model is used to investigate the influence of annually varying OH concentrations and emissions (as opposed to constant OH and emissions) on the global $\delta^{13}C_{CH_4}$ isotopic ratio. The model calculates the concentration of $^{12}CH_4$ and $^{13}CH_4$ separately and the isotopic ratio is calculated as

$$\delta^{13}C(CH_4) = \left(\frac{[^{13}CH_4]/[^{12}CH_4]}{R_{standard}} - 1 \right) \times 1000‰ \qquad (1)$$

where $R_{standard}$ is Vienna Peedee belemnite (VPDB) isotopic standard with a value of 0.011183[87].

Losses through reaction with OH, Cl and through soil uptake are accounted for. The reaction rates for OH + CH4 and Cl +CH4 are taken from NASA/JPL[88] while a lifetime of 160 years is assumed for the soil sink. A constant Cl concentration of 620 cm^{-3} is assumed based on Wang, et al.[89].

The kinetic isotope effect (KIE), representing the ratio between reaction rate with $^{13}CH_4$ and $^{12}CH_4$ ($\alpha = k_{13}/k_{12}$), is assumed $\alpha = 0.9946$ for loss through reaction with OH[90], $\alpha = 0.938$ for loss through reaction with Cl[91], and $\alpha = 0.978$ for loss through soil uptake[92].

The reference simulation with the isotopic box model has been run from 1970 to 2020 using EDGARv7 anthropogenic emissions, constant climatological biomass burning emissions of 15.73 Tg yr^{-1} (GFED mean between 1997–2021), and constant natural emissions of 215 Tg yr^{-1} as in the methane box model. Isotopic signatures and uncertainties for each emission sector are from Table S4 in Zhang, et al.[93]. The time evolution of sectoral anthropogenic emissions and the isotopic signature for the most important sectors are shown in Supplementary Fig. 11. The evolution of OH concentrations is taken from the OsloCTM3 (CEDS21 + COVID) simulation, and the initial (1970) OH concentration of 1.303e6 molec cm^{-3} is set to approximately give mass balance in 1970 for a methane mixing ratio of 1550 ppb (this methane mixing ratio is higher than observed but chosen so that the box model approximately reproduces the observed methane mixing ratios in recent years). Supplementary Fig. 10 shows the OH concentration, CH$_4$ mixing ratio and $\delta^{13}C_{CH_4}$ isotopic ratio for the reference simulation and simulations with different OH evolution.

Table 2 Overview of the main simulations performed with the isotopic box model.

Simulation	Description
REF	Reference simulation (OH time evolution from OsloCTM3, constant wetland emissions)
OH_AerChemMIP	Same as REF except OH time evolution from OsloCTM3 replaced with that from AerChemMIP
OH_CCMI	Same as REF except OH time evolution from OsloCTM3 replaced with that from CCMI
OH_constant	Same as REF except OH time evolution set to constant
Fossil_constant	Same as REF except emissions from coal, gas, oil and industry set to constant from 2007
Livestock_constant	Same as REF except emissions from livestock set to constant from 2007
Rice_constant	Same as REF except emissions from rice set to constant from 2007
Waste_constant	Same as REF except emissions from waste set to constant from 2007
CLM_GSWP3	Same as REF except wetland emission evolution from CLM GSWP3 instead of constant
CLM_CRUNCEP	Same as REF except wetland emission evolution from CLM CRUNCEP instead of constant
CLM_CRUJRA	Same as REF except wetland emission evolution from CLM CRUJRA instead of constant
Zhang23_MERRA2	Same as REF except wetland emission evolution from Zhang, et al.[21] MERRA2 instead of constant
Zhang23_CRU	Same as REF except wetland emission evolution from Zhang, et al.[21] CRU instead of constant

Several sensitivity simulations have been conducted—see Table 2. The different lines in Fig. 6 show differences between simulations, in (a) REF-OH_constant, OH_AerChemMIP-OH_constant, and OH_CCMI-OH_constant; in (b) REF-Fossil_constant, REF-Livestock_constant, REF-Rice_constant, and REF-Waste_constant; in (c) CLM_GSWP3-REF, CLM_CRUNCEP-REF, CLM_CRUJRA-REF, Zhang23_MERRA2-REF, and Zhang23_CRU-REF. In addition to the simulations in Table 2, different sets of sensitivity simulations have been performed to investigate the influence of uncertainty in the isotopic signature of individual emission sectors (shown as shading in Fig. 6b, c), and the influence of using CEDS-2021 emissions instead of EDGARv7 (shown in Supplementary Fig. 12). Also, as the modelled $\delta^{13}C_{CH_4}$ isotopic ratio is around 3.5–4‰ too negative compared to observations (Supplementary Fig. 10), a different set of simulations was carried out where the model was tuned to better match the $\delta^{13}C_{CH_4}$ isotopic ratio by increasing the (isotopically weakly negative) biomass burning emissions fivefold. The results from these simulations show a much better comparison against observed $\delta^{13}C_{CH_4}$ (Supplementary Fig. 13a) and the sensitivity simulations (Supplementary Fig. 13b–d) yield fairly similar results as those in Fig. 6, indicating that the main results (shown in Fig. 6) are fairly robust despite the underestimated isotopic ratio.

The limitations mentioned above for the methane box model apply also here for the isotopic box model. In addition, an important limitation is that one global mean value for the isotopic signature is used for each emission sector, while in reality these values differ in space and partly also in time.

Data availability

Code availability

References

1. Forster, P. et al. *The Earth's Energy Budget, Climate Feedbacks, and Climate Sensitivity in Climate Change 2021: The Physical Science Basis. Contribution of Working Group I to the Sixth Assessment Report of the Intergovernmental Panel on Climate Change* (eds. Masson-Delmotte, V. et al.) Ch. 7 (Cambridge University Press, UK 2021).
2. WMO/GAW. *WMO Greenhouse Gas Bulletin (GHG Bulletin)—No.18: The State of Greenhouse Gases in the Atmosphere Based on Global Observations Through 2021* (United Nations Office for the Coordination of Humanitarian Affairs, 2022).
3. Canadell, J. G. et al. *Global Carbon and other Biogeochemical Cycles and Feedbacks in Climate Change 2021: The Physical Science Basis. Contribution of Working Group I to the Sixth Assessment Report of the Intergovernmental Panel on Climate Change* (eds. Masson-Delmotte V. et al.) Ch. 5 (Cambridge University Press, UK, 2021).
4. Nisbet, E. G. et al. Very strong atmospheric methane growth in the 4 years 2014–2017: implications for the Paris agreement. *Global Biogeochem. Cy.* https://doi.org/10.1029/2018GB006009 (2019).
5. Ganesan, A. L. et al. Advancing scientific usderstanding of the global methane budget in support of the Paris agreement. *Glob. Biogeochem. Cy.* **33**, 1475–1512 (2019).
6. Collins, W. J. et al. Increased importance of methane reduction for a 1.5 degree target. *Environ. Res. Let.* **13**, 054003 (2018).
7. Fletcher, S. E. M. & Schaefer, H. Rising methane: a new climate challenge. *Science* **364**, 932 (2019).
8. UNFCCC. *Adoption of the Paris Agreement FCCC/CP/2015/L.9/Rev. 1.* http://unfccc.int/resource/docs/2015/cop21/eng/l09r01.pdf. (2015).
9. Lan, X., K. W. Thoning, K. W. & Dlugokencky, E. J. *Trends in Globally-averaged CH4, N2O, and SF6 Determined from NOAA Global Monitoring Laboratory Measurements.* https://doi.org/10.15138/P8XG-AA10 (2023).
10. Turner, A. J., Frankenberg, C. & Kort, E. A. Interpreting contemporary trends in atmospheric methane. *Proc. Natl Acad. Sci. USA* **116**, 2805 (2019).
11. Dlugokencky, E. J. et al. Observational constraints on recent increases in the atmospheric CH4 burden. *Geophys. Res. Lett.* https://doi.org/10.1029/2009gl039780 (2009).
12. Rigby, M. et al. Renewed growth of atmospheric methane. *Geophys. Res. Lett.* **35**, L22805 (2008).
13. Saunois, M. et al. The global methane budget 2000–2017. *Earth Syst. Sci. Data* **12**, 1561–1623 (2020).
14. Jackson, R. B. et al. Increasing anthropogenic methane emissions arise equally from agricultural and fossil fuel sources. *Environ. Res. Let.* **15**, 071002 (2020).
15. Zhang, Y. et al. Attribution of the accelerating increase in atmospheric methane during 2010–2018 by inverse analysis of GOSAT observations. *Atmos. Chem. Phys.* **21**, 3643–3666 (2021).
16. Chandra, N. et al. Emissions from the oil and gas sectors, coal mining and ruminant farming drive methane growth over the past three decades. *J. Meteorol. Soc. of Jpn. Ser. II* **99**, 309–337 (2021).
17. He, J., Naik, V., Horowitz, L. W., Dlugokencky, E. & Thoning, K. Investigation of the global methane budget over 1980–2017 using GFDL-AM4.1. *Atmos. Chem. Phys.* **20**, 805–827 (2020).
18. Höglund-Isaksson, L., Gómez-Sanabria, A., Klimont, Z., Rafaj, P. & Schöpp, W. Technical potentials and costs for reducing global anthropogenic methane emissions in the 2050 timeframe –results from the GAINS model. *Environ. Res. Commun.* **2**, 025004 (2020).
19. Paudel, R., Mahowald, N. M., Hess, P. G. M., Meng, L. & Riley, W. J. Attribution of changes in global wetland methane emissions from pre-industrial to present using CLM4.5-BGC. *Environ. Res. Let.* **11**, 034020 (2016).
20. Arora, V. K., Melton, J. R. & Plummer, D. An assessment of natural methane fluxes simulated by the CLASS-CTEM model. *Biogeosciences* **15**, 4683–4709 (2018).
21. Zhang, Z. et al. Recent intensification of wetland methane feedback. *Nat. Clim. Change* **13**, 430–433 (2023).
22. Parker, R. J. et al. Evaluating year-to-year anomalies in tropical wetland methane emissions using satellite CH4 observations. *Remote Sensing of Environ.* **211**, 261–275 (2018).
23. Oh, Y. et al. Improved global wetland carbon isotopic signatures support post-2006 microbial methane emission increase. *Commun. Earth & Environ.* **3**, 159 (2022).
24. Drinkwater, A. et al. Atmospheric data support a multi-decadal shift in the global methane budget towards natural tropical emissions. *Atmos. Chem. Phys.* **23**, 8429–8452 (2023).
25. Yin, Y. et al. Accelerating methane growth rate from 2010 to 2017: leading contributions from the tropics and East Asia. *Atmos. Chem. Phys.* **21**, 12631–12647 (2021).
26. Tunnicliffe, R. L. et al. Quantifying sources of Brazil's CH4 emissions between 2010 and 2018 from satellite data. *Atmos. Chem. Phys.* **20**, 13041–13067 (2020).
27. Wilson, C. et al. Large and increasing methane emissions from eastern Amazonia derived from satellite data, 2010–2018. *Atmos. Chem. Phys.* **21**, 10643–10669 (2021).
28. Lunt, M. F. et al. Rain-fed pulses of methane from East Africa during 2018–2019 contributed to atmospheric growth rate. *Environ. Res. Let.* **16**, 024021 (2021).
29. Lunt, M. F. et al. An increase in methane emissions from tropical Africa between 2010 and 2016 inferred from satellite data. *Atmos. Chem. Phys.* **19**, 14721–14740 (2019).
30. Szopa, S. et al. *Short-Lived Climate Forcers in Climate Change 2021: The Physical Science Basis. Contribution of Working Group I to the Sixth Assessment Report of the Intergovernmental Panel on Climate Change* (eds. Masson-Delmotte V. et al.) Ch. 6 (Cambridge University Press, UK, 2021). https://doi.org/10.1017/9781009157896.008.
31. Zhao, Y. et al. Inter-model comparison of global hydroxyl radical (OH) distributions and their impact on atmospheric methane over the 2000–2016 period. *Atmos. Chem. Phys.* **19**, 13701–13723 (2019).
32. Dalsøren, S. B. et al. Atmospheric methane evolution the last 40 years. *Atmos. Chem. Phys.* **16**, 3099–3126 (2016).

33. Stevenson, D. S. et al. Trends in global tropospheric hydroxyl radical and methane lifetime since 1850 from AerChemMIP. *Atmos. Chem. Phys.* **20**, 12905–12920 (2020).

34. Bousquet, P., Hauglustaine, D. A., Peylin, P., Carouge, C. & Ciais, P. Two decades of OH variability as inferred by an inversion of atmospheric transport and chemistry of methyl chloroform. *Atmos. Chem. Phys.* **5**, 2635–2656 (2005).

35. Montzka, S. A. et al. Small interannual variability of global atmospheric hydroxyl. *Science* **331**, 67–69 (2011).

36. Rigby, M. et al. Role of atmospheric oxidation in recent methane growth. *PNAS* **114**, 5373 (2017).

37. Turner, A. J., Frankenberg, C., Wennberg, P. O. & Jacob, D. J. Ambiguity in the causes for decadal trends in atmospheric methane and hydroxyl. *PNAS* **114**, 5367 (2017).

38. Patra, P. K. et al. Methyl chloroform continues to constrain the Hydroxyl (OH) variability in the troposphere. *J. Geophys. Res.* **126**, e2020JD033862 (2021).

39. Zhao, Y. et al. On the role of trend and variability in the hydroxyl radical (OH) in the global methane budget. *Atmos. Chem. Phys.* **20**, 13011–13022 (2020).

40. Nguyen, N. H., Turner, A. J., Yin, Y., Prather, M. J. & Frankenberg, C. Effects of chemical feedbacks on decadal methane emissions estimates. *Geophys. Res. Lett.* **47**, e2019GL085706 (2020).

41. Meinshausen, M. et al. Historical greenhouse gas concentrations for climate modelling (CMIP6). *Geosci. Model Dev.* **10**, 2057–2116 (2017).

42. Morgenstern, O. et al. Review of the global models used within phase 1 of the Chemistry–Climate Model Initiative (CCMI). *Geosci. Model Dev.* **10**, 639–671 (2017).

43. Collins, W. J. et al. AerChemMIP: quantifying the effects of chemistry and aerosols in CMIP6. *Geosci. Model Dev.* **10**, 585–607 (2017).

44. Lamarque, J. F. et al. Historical (1850–2000) gridded anthropogenic and biomass burning emissions of reactive gases and aerosols: methodology and application. *Atmos. Chem. Phys.* **10**, 7017–7039 (2010).

45. Riahi, K. et al. RCP 8.5—A scenario of comparatively high greenhouse gas emissions. *Clim. Change* **109**, 33–57 (2011).

46. Stevenson, D. S., Derwent, R. G., Wild, O. & Collins, W. J. COVID-19 lockdown emission reductions have the potential to explain over half of the coincident increase in global atmospheric methane. *Atmos. Chem. Phys.* **22**, 14243–14252 (2022).

47. Peng, S. et al. Wetland emission and atmospheric sink changes explain methane growth in 2020. *Nature* **612**, 477–482 (2022).

48. Müller, J. et al. CH₄ parameter estimation in CLM4.5bgc using surrogate global optimization. *Geosci. Model Dev.* **8**, 3285–3310 (2015).

49. Zhang, Z. et al. Development of the global dataset of Wetland Area and Dynamics for Methane Modeling (WAD2M). *Earth Syst. Sci. Data* **13**, 2001–2023 (2021).

50. Poulter, B. et al. Global wetland contribution to 2000–2012 atmospheric methane growth rate dynamics. *Environ. Res. Let.* **12**, 094013 (2017).

51. Sherwood, O. A., Schwietzke, S., Arling, V. A. & Etiope, G. Global Inventory of Gas Geochemistry Data from Fossil Fuel, Microbial and Burning Sources, version 2017. *Earth Syst. Sci. Data* **9**, 639–656 (2017).

52. Haghnegahdar, M. A., Schauble, E. A. & Young, E. D. A model for ¹²CH₂D₂ and ¹³CH₃D as complementary tracers for the budget of atmospheric CH₄. *Global Biogeochem. Cy* **31**, 1387–1407 (2017).

53. Stell, A. C., Western, L. M., Sherwen, T. & Rigby, M. Atmospheric-methane source and sink sensitivity analysis using Gaussian process emulation. *Atmos. Chem. Phys.* **21**, 1717–1736 (2021).

54. Ganesan, A. L. et al. Spatially resolved isotopic source signatures of wetland methane emissions. *Geophys. Res. Lett.* **45**, 3737–3745 (2018).

55. Solazzo, E. et al. Uncertainties in the Emissions Database for Global Atmospheric Research (EDGAR) emission inventory of greenhouse gases. *Atmos. Chem. Phys.* **21**, 5655–5683 (2021).

56. Minx, J. C. et al. A comprehensive and synthetic dataset for global, regional, and national greenhouse gas emissions by sector 1970–2018 with an extension to 2019. *Earth Syst. Sci. Data* **13**, 5213–5252 (2021).

57. Forster, P. M. et al. Current and future global climate impacts resulting from COVID-19. *Nature Climate Change* **10**, 913–919 (2020).

58. McNorton, J. et al. Quantification of methane emissions from hotspots and during COVID-19 using a global atmospheric inversion. *Atmos. Chem. Phys.* **22**, 5961–5981 (2022).

59. Laughner, J. L. et al. Societal shifts due to COVID-19 reveal large-scale complexities and feedbacks between atmospheric chemistry and climate change. *PNAS* **118**, e2109481118 (2021).

60. Pandey, S. et al. Satellite observations reveal extreme methane leakage from a natural gas well blowout. *Proc. Natl Acad. Sci. USA* **116**, 26376 (2019).

61. Holmes, C. D., Prather, M. J., Søvde, O. A. & Myhre, G. Future methane, hydroxyl, and their uncertainties: key climate and emission parameters for future predictions. *Atmos. Chem. Phys.* **13**, 285–302 (2013).

62. Naik, V. et al. Preindustrial to present-day changes in tropospheric hydroxyl radical and methane lifetime from the Atmospheric Chemistry and Climate Model Intercomparison Project (ACCMIP). *Atmos. Chem. Phys.* **13**, 5277–5298 (2013).

63. Nicely, J. M. et al. Changes in global tropospheric OH expected as a result of climate change over the last several decades. *J. Geophys. Res.* **123**, 10,774–710,795 (2018).

64. McNorton, J. et al. Role of OH variability in the stalling of the global atmospheric CH₄ growth rate from 1999 to 2006. *Atmos. Chem. Phys.* **16**, 7943–7956 (2016).

65. Hoesly, R. M. et al. Historical (1750–2014) anthropogenic emissions of reactive gases and aerosols from the Community Emissions Data System (CEDS). *Geosci. Model Dev.* **11**, 369–408 (2018).

66. Lan, X. et al. Improved constraints on global methane emissions and sinks using δ13C-CH4. *Global Biogeochem. Cy.* **35**, e2021GB007000 (2021).

67. Søvde, O. A. et al. The chemical transport model Oslo CTM3. *Geosci. Model Dev.* **5**, 1441–1469 (2012).

68. Lund, M. T. et al. Concentrations and radiative forcing of anthropogenic aerosols from 1750 to 2014 simulated with the Oslo CTM3 and CEDS emission inventory. *Geosci. Model Dev.* **11**, 4909–4931 (2018).

69. van Marle, M. J. E. et al. Historic global biomass burning emissions for CMIP6 (BB4CMIP) based on merging satellite observations with proxies and fire models (1750–2015). *Geosci. Model Dev.* **10**, 3329–3357 (2017).

70. Fricko, O. et al. The marker quantification of the Shared Socioeconomic Pathway 2: a middle-of-the-road scenario for the 21st century. *Glob. Environ. Change* **42**, 251–267 (2017).

71. van der Werf, G. R. et al. Global fire emissions estimates during 1997–2016. *Earth Syst. Sci. Data* **9**, 697–720 (2017).

72. O'Rourke et al. CEDS v_2021_04_21 Release Emission Data (v_2021_02_05). *Zenodo* https://doi.org/10.5281/zenodo.4741285 (2021).

73. Lamboll, R. D. et al. Modifying emissions scenario projections to account for the effects of COVID-19: protocol for CovidMIP. *Geosci. Model Dev.* **14**, 3683–3695 (2021).

74. Forster, P., Lamboll, R. & Rogelj, J. Emissions changes in 2020 due to Covid19 (5.1). *Zenodo* https://doi.org/10.5281/zenodo.4603979 (2021).

75. Lawrence, D. M. et al. The community land model version 5: description of new features, benchmarking, and impact of forcing uncertainty. *J. Adv. Model. Earth Syst.* https://doi.org/10.1029/2018MS001583 (2019).

76. Danabasoglu, G. et al. The Community Earth System Model Version 2 (CESM2). *J. Adv. Model. Earth Syst.* **12**, e2019MS001916 (2020).

77. Meng, L. et al. Sensitivity of wetland methane emissions to model assumptions: application and model testing against site observations. *Biogeosciences* **9**, 2793–2819 (2012).

78. Riley, W. J. et al. Barriers to predicting changes in global terrestrial methane fluxes: analyses using CLM4Me, a methane biogeochemistry model integrated in CESM. *Biogeosciences* **8**, 1925–1953 (2011).

79. Lawrence, D. M. et al. *Technical Description of version 5.0 of the Community Land Model (CLM)* (National Center for Atmospheric Research, 2018).

80. FAO/IIASA/ISRIC/ISSCAS/JRC. *Harmonized World Soil Database (version 1.2)* https://www.fao.org/soils-portal/data-hub/soil-maps-and-databases/harmonized-world-soil-database-v12/en/ (2012).

81. Bonan, G. B. et al. Model structure and climate data uncertainty in historical simulations of the terrestrial carbon cycle (1850–2014). *Global Biogeochem. Cy.* **33**, 1310–1326 (2019).

82. University of East Anglia Climatic Research Unit; Harris, I. C. CRU JRA v2.1: A Forcings Dataset of Gridded Land Surface Blend of Climatic Research Unit (CRU) and Japanese Reanalysis (JRA) Data. https://catalogue.ceda.ac.uk/uuid/10d2c73e5a7d46f4ada08b0a26302ef7 (2020).

83. Trenberth, K. E. & Smith, L. The mass of the atmosphere: a constraint on global analyses. *J. Clim.* **18**, 864–875 (2005).

84. Stevenson, D. S. et al. Tropospheric ozone changes, radiative forcing and attribution to emissions in the Atmospheric Chemistry and Climate Model Intercomparison Project (ACCMIP). *Atmos. Chem. Phys.* **13**, 3063–3085 (2013).

85. GFED. *Global Fire Emissions Database Version 4.1 Including Small Fire Burned Area (GFED4s).* https://www.geo.vu.nl/~gwerf/GFED/GFED4/tables/GFED4.1s_CH4.txt (2022).

86. Zhang, Z. *Global Wetland CH4 Emissions for 2000–2021.* https://doi.org/10.5281/zenodo.7595223 (2023).

87. Zhang, Q.-L. & Li, W.-J. A calibrated measurement of the atomic weight of carbon. *Chinese Sci. Bull.* **35**, 290–296 (1990).

88. Burkholder, J. B. et al. *Chemical Kinetics and Photochemical Data for Use in Atmospheric Studies, Evaluation No. 19.* http://jpldataeval.jpl.nasa.gov (2019).

89. Wang, X. et al. The role of chlorine in global tropospheric chemistry. *Atmos. Chem. Phys.* **19**, 3981–4003 (2019).

90. Cantrell, C. A. et al. Carbon kinetic isotope effect in the oxidation of methane by the hydroxyl radical. *J. Geophys. Res.* **95**, 22455–22462 (1990).

91. Saueressig, G., Bergamaschi, P., Crowley, J. N., Fischer, H. & Harris, G. W. Carbon kinetic isotope effect in the reaction of CH₄ with Cl atoms. *Geophys. Res. Lett.* **22**, 1225–1228 (1995).

92. Tyler, S. C., Crill, P. M. & Brailsford, G. W. $^{13}C^{12}C$ Fractionation of methane during oxidation in a temperate forested soil. *Geochim. Cosmochim. Acta* **58**, 1625–1633 (1994).

93. Zhang, Z. et al. Anthropogenic emission is the main contributor to the rise of atmospheric methane during 1993–2017. *Natl Sci. Rev.* https://doi.org/10.1093/nsr/nwab200 (2022).

94. McDuffie, E. E. et al. A global anthropogenic emission inventory of atmospheric pollutants from sector- and fuel-specific sources (1970–2017): an application of the Community Emissions Data System (CEDS). *Earth Syst. Sci. Data* **12**, 3413–3442 (2020).

95. Gidden, M. J. et al. Global emissions pathways under different socioeconomic scenarios for use in CMIP6: a dataset of harmonized emissions trajectories through the end of the century. *Geosci. Model Dev.* **12**, 1443–1475 (2019).

96. van Vuuren, D. P. et al. The representative concentration pathways: an overview. *Clim. Change* **109**, 5 (2011).

97. Crippa, M. et al. *CO2 Emissions of All World Countries—2022 Report, EUR 31182 EN* (Publications Office of the European Union, Luxembourg, 2022).

98. EC-JRC/PBL. *Emissions Database for Global Atmospheric Research (EDGAR).* https://edgar.jrc.ec.europa.eu/ (2021).

99. Crippa, M. et al. *Fossil CO2 and GHG Emissions of All World Countries—2019 Report, EUR 29849 EN* (Publications Office of the European Union, Luxembourg, 2019).

100. Schaefer, H. et al. A 21st-century shift from fossil-fuel to biogenic methane emissions indicated by $^{13}CH_4$. *Science* **352**, 80–84 (2016).

101. Whaley, C. H. et al. Model evaluation of short-lived climate forcers for the arctic monitoring and assessment programme: a multi-species, multi-model study. *Atmos. Chem. Phys.* **22**, 5775–5828 (2022).

Author contributions

R.B.S. lead the work and wrote the paper. R.B.S. performed the OsloCTM3 simulations, CLM simulations and box model simulations. Ø.H. did the isotopic box model simulations. G.M. and Ø.H. gave input and contributed to the writing.

Competing interests

The authors declare no competing interests.

Additional information

Supplementary information The online version contains supplementary material available at https://doi.org/10.1038/s43247-023-00969-1.

Correspondence and requests for materials should be addressed to Ragnhild Bieltvedt Skeie.

Peer review information *Communications Earth & Environment* thanks the anonymous reviewers for their contribution to the peer review of this work. Primary Handling Editors: Joshua Dean, Clare Davis, Aliénor Lavergne. A peer review file is available.

Reprints and permission information is available at http://www.nature.com/reprints

Publisher's note Springer Nature remains neutral with regard to jurisdictional claims in published maps and institutional affiliations.